nature communications

Article

https://doi.org/10.1038/s41467-026-71214-4

Emerging energy signals advance early warnings of extreme precipitation

Received: 8 October 2025

Accepted: 17 March 2026

Published online: 28 March 2026

Check for updates

Tuantuan Zhang[1,2] ✉, Junwen Chen[3], Yi Deng[4] ✉, Song Yang[1,2], Deliang Chen[5], Junjie Zhu[1,2] & Fenying Cai[6,7]

The increasing frequency and intensity of extreme precipitation events pose growing societal risks, underscoring the urgent need for effective early warning systems. Forecasting such events at subseasonal-to-seasonal timescales, however, remains a major scientific challenge. Utilizing Seasonal Forecast System version 5 from the European Centre for Medium-Range Weather Forecasts, here we show that introducing a total atmospheric energy proxy into forecasts substantially improves extreme precipitation prediction at subseasonal and longer timescales. This approach extends the effective forecast lead times from about one month by conventional methods to six months, and achieves more than tenfold increases in global prediction accuracy over the past two decades. The added predictive value of total energy has increased substantially in recent years, reflecting a strengthening relationship between total energy and extreme precipitation. These findings highlight the emerging energy signals that enhance predictability, offering promising opportunities for developing more reliable early warning systems in a warming future.

Widespread increases in the frequency and intensity of extreme precipitation are amplifying the risks of catastrophic disasters such as floods and landslides, posing mounting threats to public safety and economic stability[1–8]. For example, the 2022 Pakistan floods—triggered by record-breaking extreme precipitation—resulted in over 1,700 deaths and an estimated $40 billion in damages[9–11]. These risks intensified in 2024, which ranked among the wettest years on record[12,13]. As climate projections indicate continued intensification of extreme events[14,15], the demand for effective early warning systems has never been greater.

Developing reliable early warning systems for extreme events remains a major scientific challenge, particularly at subseasonal timescale and beyond[16,17]. Traditional dynamical forecast models exhibit limited skill beyond two weeks, with predictions quickly reverting toward climatological means and failing to capture high-impact anomalies[16–20]. Recent advances in artificial intelligence (AI) have improved the forecasting of extreme precipitation at both weather and subseasonal-to-seasonal timescales[21–26], but key limitations persist. The predictive skill of both dynamical and data-driven AI systems remains constrained by the representation of key drivers, such as the Madden–Julian Oscillation, whose influence typically fades beyond 40 days[17,21,27–29]. As a result, most existing early warning systems provide limited guidance at lead times longer than 1–2 months, leaving critical gaps in disaster preparedness.

The Clausius-Clapeyron relationship suggests that a warmer atmosphere holds more moisture—roughly a 7% increase in moisture per degree of warming, contributing to more intense precipitation events[30–34]. Focusing on certain regions and cases, recent studies have shown that water vapor-related variables may offer greater predictability than precipitation itself, and can thus serve as useful

[1]School of Atmospheric Sciences, Sun Yat-sen University; and Southern Marine Science and Engineering Guangdong Laboratory (Zhuhai), Zhuhai, China. [2]Guangdong Province Key Laboratory for Climate Change and Natural Disaster Studies, Sun Yat-sen University, Zhuhai, China. [3]Shenzhen Wiselec Technology Co., Ltd., Shenzhen, China. [4]School of Earth and Atmospheric Sciences, Georgia Institute of Technology, Atlanta, GA, USA. [5]Department of Earth System Sciences, Tsinghua University, Beijing, China. [6]Potsdam Institute for Climate Impact Research (PIK), Potsdam, Germany. [7]Department of Geography, Humboldt-Universität zu Berlin, Berlin, Germany. ✉e-mail: zhangtt75@mail.sysu.edu.cn; yi.deng@eas.gatech.edu

proxies[35–38]. However, given the complex thermodynamics and dynamics involved in the occurrences of extreme precipitation[39–41], a model's skill in predicting such events depends on its capability to represent processes more than just moisture. The key processes leading to the formation of extremes often include and are not limited to moisture transport, atmospheric dynamics, radiation, land-atmosphere coupling, and cloud microphysics[32–37,39–41]. The myriad factors at play here demand a proxy of extreme precipitation that is comprehensive in encapsulating the general condition of the atmosphere. Atmospheric total energy appears to be a candidate here since it integrates latent, internal, geopotential, and kinetic energy, which offers a physically grounded measure of both dynamic and thermodynamic conditions, and is also closely linked to the hydrological cycle and phase transitions of water species[42–44]. In a warming climate, the recharge and discharge of total energy are expected to play an increasingly important role in driving extremes[44,45]. Whether this total energy signal can be harnessed to improve predictability and support early warnings, however, remains an open question.

Here, we show that introducing total energy as a proxy into forecasts can achieve superior skills for extreme precipitation at sub-seasonal scale and beyond, from regional events such as the 2022 Pakistan floods to global-scale assessments. Over the period 2005–2024, forecasts based on total energy achieved global improvements in hit rate of 372%, 2500%, and 1000% over conventional precipitation-based forecasts at lead times of 0–2, 1–3, and 2–4 months, respectively. Notably, the predictive skill of the total energy-based approach has increased over time in a warming climate.

Results

Total energy boosts early warning skill

Recent surges in extreme precipitation across the Pakistan-rim have underscored the region's growing vulnerability to climate-related disasters[9,10]. Situated on the Asian monsoon fringe, the Pakistan-rim experiences climate extremes that are intrinsically linked to those in other regions, such as Europe and East Asia, due to prevailing extra-tropical synoptic weather systems, variabilities in monsoonal circulations, and the interaction between the two[9,46–48]. This intrinsic complexity severely limits the predictive skill for extreme precipitation in the region[20,49]. To explore the potential of improved early warning, we begin with examining the relationship between extreme precipitation and atmospheric total energy in this region. Given that most extreme events occur during peak summer (July–August), our analysis focuses on this season.

The Pakistan-rim emerges as a hotspot for both precipitation and total energy variability (Fig. 1a–b), with both variables showing clear upward trends since the early 2000s (Fig. 1c). Total energy closely tracks precipitation over the past two decades, with a strong correlation ($R = 0.89$, $p < 0.001$; Fig. 1c). Using a threshold of +0.5 standard deviations, four extreme precipitation years—2010, 2020, 2022, and 2024—are identified, all of which coincide with extreme total energy years dominated by latent energy anomalies (Fig. 1c and Supplementary Fig. S1). Prior to 2000, the relationship is notably weaker ($R = 0.62$), with false alarms of 1983 and 1994 in total energy measures. The enhanced post-2000 relationship ($R = 0.83$ for 2005–2024 vs. $R = 0.55$ for 1981–2000) also holds for extreme days (defined as values above the 95th percentile) of precipitation and total energy (Fig. 1d). Such a significant relationship between precipitation and total energy is consistently observed across multiple datasets (Supplementary Fig. S2), which attests to the robustness of the findings. Given this strengthened linkage and the improved quality of reanalysis datasets after 2000 (see Methods), the subsequent analysis is focused on the period 2005–2024.

Using outputs from the European Centre for Medium-Range Weather Forecasts (ECWMF) Seasonal Forecast System version 5 (SEAS5), we compare direct precipitation predictions with those

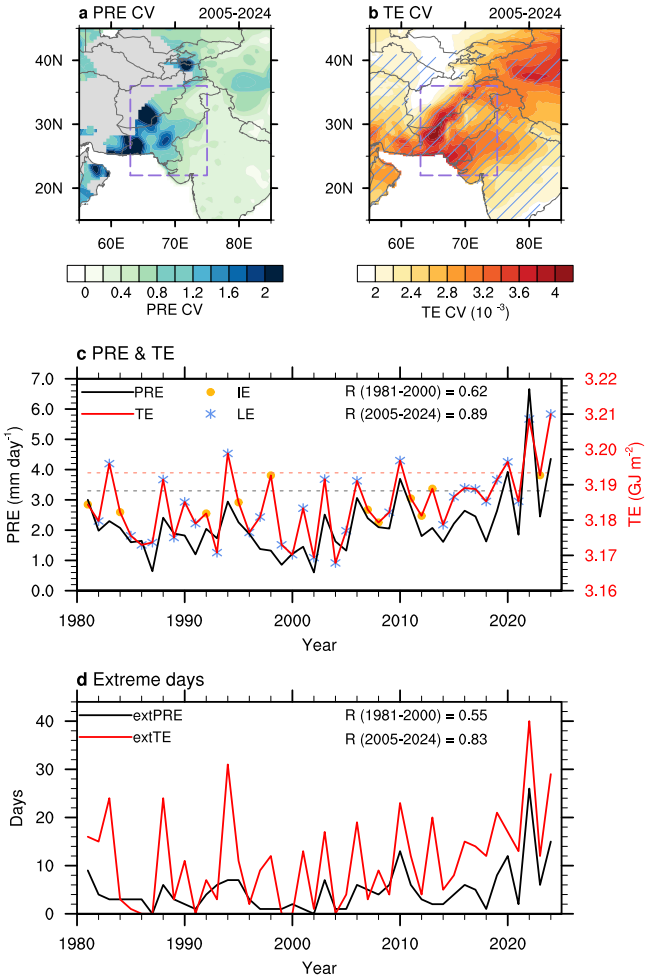


Fig. 1 | Relationship between total energy and extreme precipitation over the Pakistan-rim. Coefficient of variation (CV; the ratio of standard deviation to climatological mean) of precipitation (**a**) and total energy (10^{-3}; **b**) during peak summer (July–August) from 2005 to 2024. The Pakistan-rim region (22°–36°N, 63°–75°E) is outlined by purple rectangles. Hatched areas in (**b**) indicate regions where variance in total energy is primarily dominated by latent energy. **c** Time series of area-averaged peak-summer precipitation (mm day^{-1}; black) and total energy (GJ m^{-2}; red) over the Pakistan-rim. The peak-summer precipitation is the two-month (July and August) average precipitation. Horizontal dashed lines denote thresholds (+0.5 standard deviations) used to define extreme years. Blue stars and yellow circles mark years when total energy anomalies are dominated by latent energy and internal energy contributions, respectively. **d** Time series of extreme precipitation days (black) and extreme total energy days dominated by latent energy anomalies (red) over the Pakistan-rim during peak summer. "R" denotes the correlation coefficient between the two time series for different periods. The abbreviations "PRE", "TE", "IE", "LE", "extPRE", and "extTE", denote precipitation, total energy, internal energy, latent energy, extreme precipitation days, and extreme total energy days, respectively.

derived from total energy proxy. While the direct forecasts of regional-mean precipitation maintain significant correlation skills up to 3–4 months lead (solid blue line in Fig. 2a), the predicted precipitation variability diminishes rapidly as the lead time increases (Supplementary Figs. S4–S5), leading to a collapse in predicted extreme precipitation days beyond 0–1 month (blue star in Fig. 2a and Supplementary Fig. S6). By contrast, the predicted total energy, as a proxy of precipitation, maintains substantial variability across the forecast horizon, extending effective predictions for both regional-mean precipitation and the frequency of extreme precipitation days to 5–6 months lead—the maximum integration period of the model (Fig. 2a and Supplementary Figs. S4–6). To determine whether the

https://doi.org/10.1038/s41467-026-71214-4

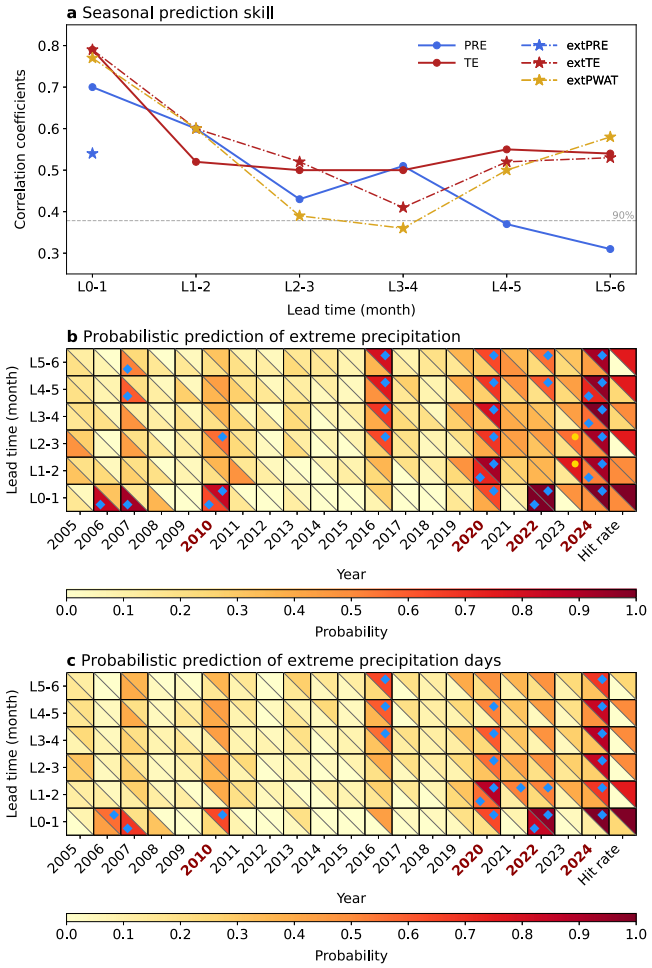


Fig. 2 | Total energy proxy improves prediction of extreme precipitation over the Pakistan-rim. a Correlation coefficients between observations and model predictions in peak summer (totally 20 samples: 2005–2024) over the Pakistan-rim. Solid lines with filled circles show correlations between observed and predicted precipitation (blue) and between observed precipitation and predicted total energy (red). Dashed lines with pentagrams show correlations between the number of observed extreme precipitation days with the number of predicted extreme precipitation days (blue), extreme precipitable water days (yellow), and extreme total energy days dominated by latent energy (red). The horizontal dashed line marks the 90% confidence threshold. Probabilistic prediction of the extreme years selected based on seasonal-mean precipitation (**b**) and the number of extreme precipitation days (**c**). Each matrix cell corresponds to a specific year and lead time. Lower-left triangles show direct predicted precipitation; upper-right triangles use predicted total energy as a proxy for precipitation. Red labels indicate observed extreme years. Blue diamonds denote strong model agreement (>50% of ensemble members) on extreme precipitation years (hits); yellow circles indicate strong model agreement on extreme heat years (dominated by internal energy). The rightmost column summarizes the extreme-year hit rates. Lead times are defined based on the shortest and longest time intervals between initialization and target months. The abbreviations "L0–1", "L1–2", "L2–3", "L3–4", "L4–5", and "L5–6" denote 0–1 months leads, 1–2 months leads, 2–3 months leads, 3–4 months leads, 4–5 months leads, and 5–6 months leads, respectively.

enhanced skill is solely derived from moisture processes, the prediction skill using precipitable water as a proxy is examined. While this proxy performs comparably to total energy at short lead times (2–3 months), its skill rapidly degrades thereafter (Fig. 2a), suggesting that other processes encapsulated in total energy (e.g., dynamics, radiative heating, convective motions) also contributed to the enhanced predictability.

Since early warning systems are designed primarily for high-impact event preparedness, we further assess prediction skill for extreme years (see Methods and Supplementary Fig. S3 for details). Here we leverage probabilistic predictions from ensemble members as the ensemble mean tends to average out predictions. Direct precipitation forecasts show limited reliability, correctly identifying only two extreme years (2010 and 2022) based on regional-mean precipitation (Fig. 2b), and only one (2022) based on the frequency of extreme precipitation days (Fig. 2c) at 0–1 month lead, along with multiple false alarms. At longer leads, hit rates fall to near zero (Fig. 2b, c). In contrast, forecasts based on total energy successfully capture nearly all extreme years at 0–1 month with no false alarms, and outperform direct precipitation forecasts across all lead times. Notably, the total energy proxy successfully predicts the 2020 and 2024 extremes up to 5–6 months ahead (Fig. 2b–c), demonstrating its strong potential for early warning applications.

Subseasonal predictability

Subseasonal prediction plays a critical role in achieving seamless weather-to-climate forecasting. However, this timescale is often described as a "predictability desert"—particularly for extreme precipitation—due to rapidly diminishing forecast skill. Among the years examined, 2022 stands out as the most severe extreme precipitation year over the Pakistan-rim (Fig. 1c, d). Yet, despite its intensity, forecasts based on total energy showed only modest improvements in predictive skill that year compared to other extremes (Fig. 2b, c), making it a valuable candidate for examining the dynamical limits of subseasonal predictability.

Using ECMWF ensemble mean forecasts initialized on 1 July and 1 August (0–1 month lead), we assess both total energy-based and direct precipitation predictions. Neither approach successfully reproduces the daily precipitation evolution (Fig. 3a), which is expected as this falls within the domain of short-range weather forecasting. However, the total energy-based probabilistic forecast highlights elevated risk levels throughout July (Fig. 3a, c). In contrast, direct precipitation forecasts initialized on 1 July detect only a brief high-risk window during July 6–9, showing little skill beyond weather scales (Fig. 3a, c). In August, total energy-based predictions outperform direct forecasts but still struggle to retain skill beyond two weeks (Fig. 3a, c).

To better understand the underlying limits of predictability in 2022, we diagnose the total energy budget (see Methods), providing physical insight into forecast breakdowns. Figure 3b shows the fraction of ensemble members that reproduce the observed sign of anomalies for different total energy budget terms. For the 1 July initialization, the consistency between predicted and observed total energy tendencies drops below 50% after two weeks; for the 1 August initialization, the decline occurs within one week (Fig. 3b, Supplementary Fig. S7a). This loss of skill is mainly driven by errors in the atmospheric dynamics term (Fig. 3b, Supplementary Fig. S7b), with model-simulated anomalous circulation patterns diverging markedly from observations beyond two weeks in July and one week in August (Supplementary Fig. S8). The particularly low predictability in August may partly attributable to multiple tropical disturbances propagating across the region from east to west[50].

From an energy-budget perspective, both radiative heating and surface heat flux terms show higher levels of predictability at subseasonal timescale (Fig. 3b, Supplementary Fig. S7c–e). Notably, the radiative predictability primarily stems from longwave radiation rather than shortwave components in this case (Supplementary Fig. S9a, b). The radiative effects of precipitable water offer an additional source of subseasonal predictability (Supplementary Fig. S9d), explaining partly why total energy-based forecasts outperform predictions based on precipitable water alone. Meanwhile, surface sensible and latent heat fluxes exhibit strong agreement between model and observations across the entire forecast period, highlighting the comparatively high subseasonal predictability of land surface processes, at least for the 2022 case (Fig. 3b, Supplementary Figs. S7d–e, 9e–f).

https://doi.org/10.1038/s41467-026-71214-4

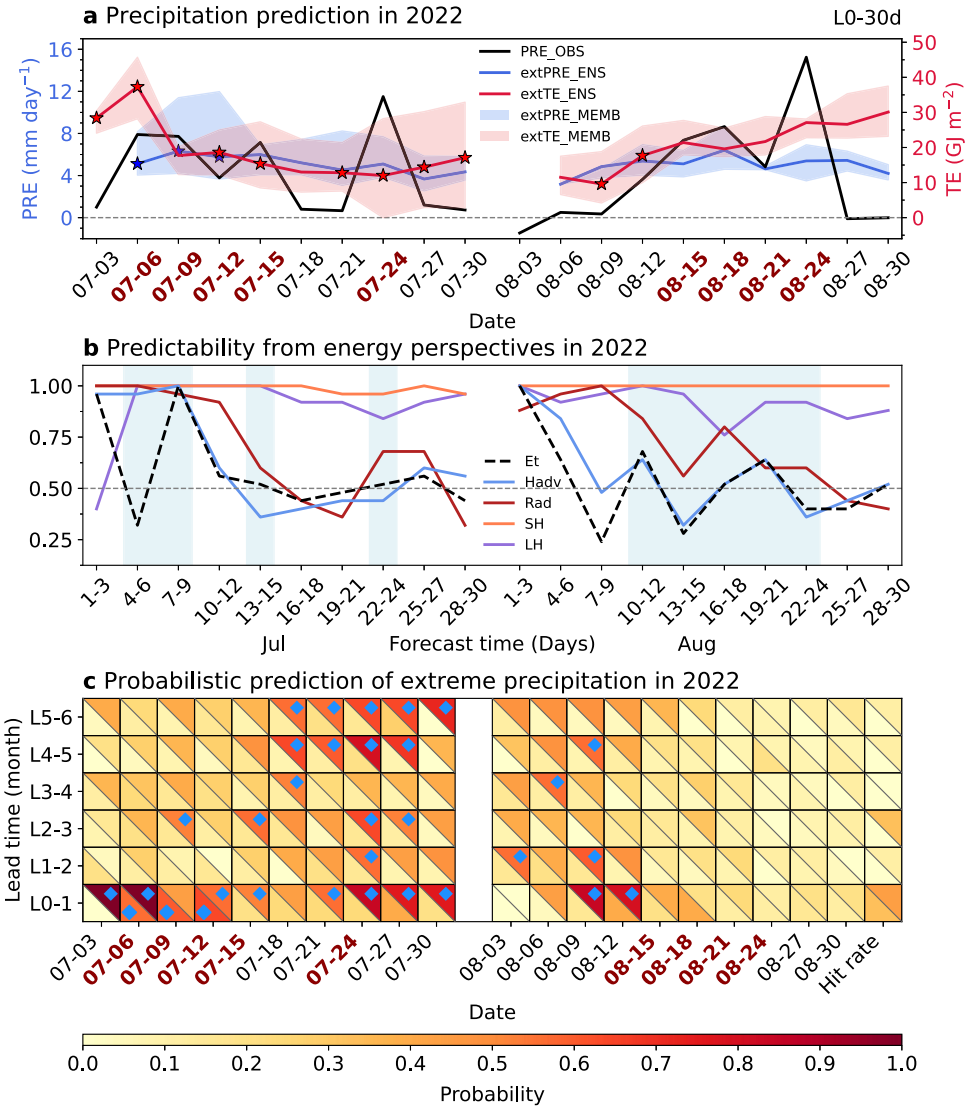


Fig. 3 | Subseasonal prediction of extreme precipitation from a total energy perspective. a Time series of observed (black) and predicted 3-day mean extreme precipitation (mm day^{-1}; blue), and predicted 3-day mean extreme total energy (GJ m^{-2}; red) over the Pakistan-rim during the 2022 peak summer. Left and right panels show forecasts initialized on 1 July (targeting 1–31 July) and 1 August (targeting 1–31 August), respectively. Red labels mark observed extreme precipitation days. Pentagrams indicate high model consensus (>50% of ensemble members) on extreme precipitation days (hits). Shaded areas (red and blue) show the range among ensemble members exceeding the extreme threshold. The abbreviations "PRE", "TE", and "L0–30 d" denote precipitation, total energy, and lead time of 0–30 days, respectively. **b** Agreement rate among ensemble members on the sign of total energy budget terms, including total energy tendency (dashed black), horizontal advection (blue), radiative heating (red), surface sensible heat flux (orange), and surface latent heat flux (purple). Light blue shading highlights periods of extreme precipitation. The dashed horizontal line marks 50% ensemble agreement. **c** Same as in Fig. 2b, but for daily precipitation prediction. Red labels indicate observed extreme days. Blue diamonds denote strong model agreement (>50% of ensemble members) on extreme precipitation days (hits). The abbreviations "L0–1", "L1–2", "L2–3", "L3–4", "L4–5", and "L5–6" denote 0–1 months leads, 1–2 months leads, 2–3 months leads, 3–4 months leads, 4–5 months leads, and 5–6 months leads, respectively.

Emerging global total energy signals

To evaluate the broader applicability of the total energy-based prediction, we assess global hit rates for extreme years selected by seasonal-mean precipitation (Fig. 4a–c) and the frequency of extreme precipitation days (Fig. 4d–f) (see "Methods"). To align with operational forecasting needs, we focus on predictions initialized on 1 July (0–2 months lead), 1 June (1–3 months lead), and 1 May (2–4 months lead), covering the full peak summer. Across all lead times, total energy-based forecasts consistently outperform traditional precipitation-based predictions, particularly for extreme precipitation days (Fig. 4). Compared to direct precipitation forecasts, the total energy proxy increases the global hit rate for extreme precipitation days by 372%, 2500%, and 1000% for 0–2, 1–3, and 2–4 months lead, respectively (Supplementary Table S1). For seasonal-mean precipitation, the improvements are 39%, 64%, and 84% over the same periods (Supplementary Table S1). Such pronounced improvement is also evident when employing other verification metrics, such as the Critical Success Index (CSI) and Heidke Skill Score (HSS) (Supplementary Figs. S10–11 and Table S1). The 2022 case provides a clear example: total energy anomalies closely align with extreme precipitation distributions globally and capture more hit grids than direct forecasts (Fig. 5), providing a physical basis for incorporating the total energy proxy into operational forecasting. The spatial coherence of extreme total energy pattern also exceeds that of precipitation (Fig. 5a and c), indicating greater predictability potential of the former.

Notably, the predictive advantage of total energy has increased over time. The incremental skill shows a marked upward trend, particularly after the early 2010s (Fig. 4; Supplementary Figs. S10–11). In

https://doi.org/10.1038/s41467-026-71214-4

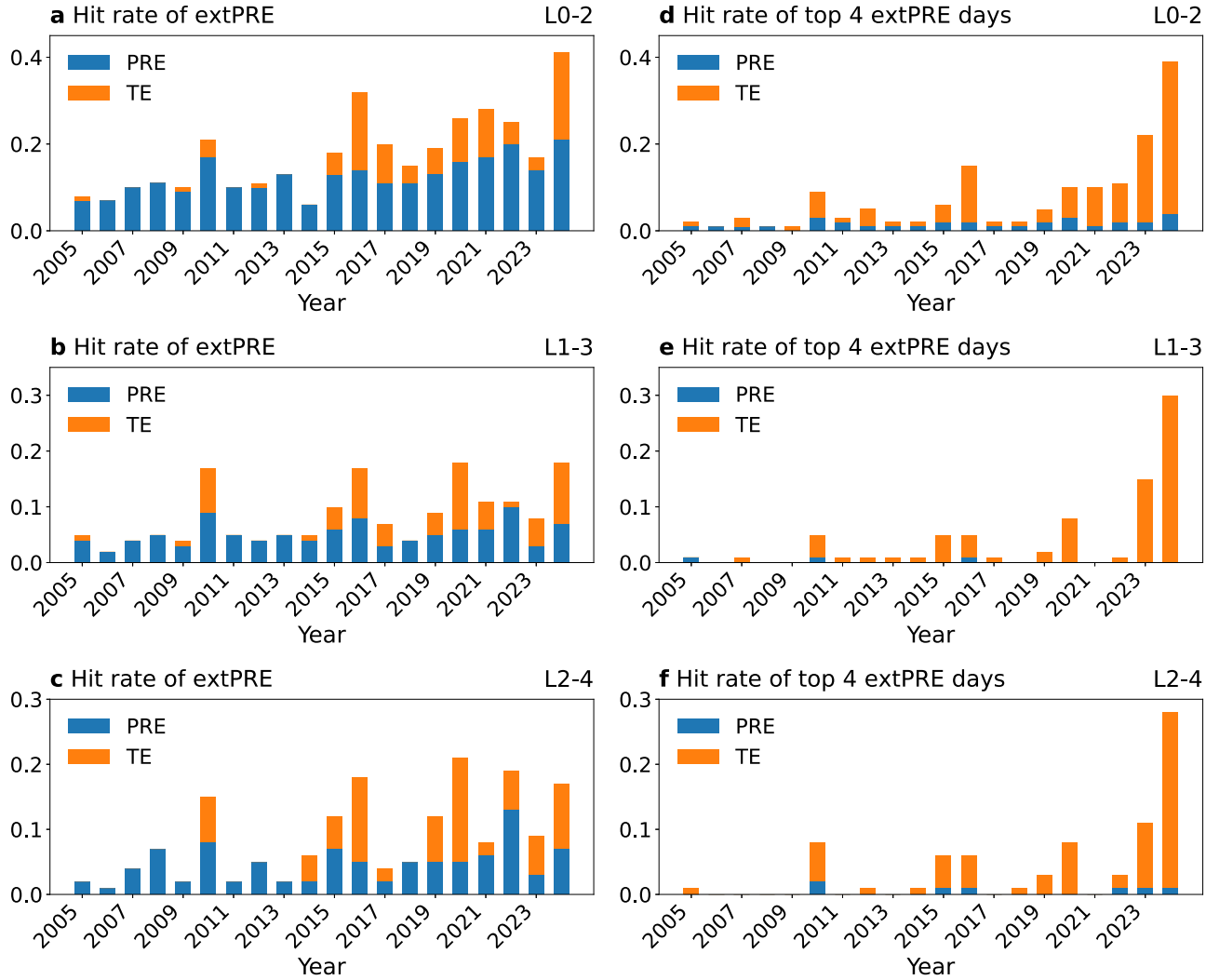


Fig. 4 | Emerging total energy signals enhance global prediction of extreme precipitation. a–c Annual global hit rates for extreme precipitation events during peak summer (July–August), using forecasts initialized on 1 July (0–2 months lead) (**a**), 1 June (1–3 months lead) (**b**), and 1 May (2–4 months lead) (**c**). Blue bars show hit rates based on direct model precipitation predictions; orange bars show hit rates improved by incorporating total energy as a predictor. Hit rate is defined as the proportion of grid cells with successful predictions (model consensus >50%) among all grid cells experiencing observed extreme precipitation. **d–f** Same as (**a–c**), but for predictions for extreme precipitation days. A year is defined as extreme when the number of extreme precipitation days ranks in the top four for the period 2005–2024. The abbreviations "PRE", "TE", and "extPRE" denote precipitation, total energy, and extreme precipitation, respectively. The abbreviations "L0–2", "L1–3", and "L2–4" denote 0–2 months leads, 1–3 months leads, and 2–4 months leads, respectively.

2024—the most recent year analyzed—direct forecasts yield almost no skill, while total energy-based predictions maintain a ~ 30% global hit rate for extreme precipitation days even at 2–4 months lead (Fig. 4d–f). A comparable advantage is also reflected by both the CSI and HSS metrics (Supplementary Fig. S10d–f and Fig. S11d–f). This improvement likely reflects rising total energy levels over land areas and the intensification of large-scale precipitation extremes in recent years (Supplementary Figs. S12–13). These results highlight emerging physically grounded signals in total energy that can be leveraged to extend the predictability horizon for extreme precipitation, offering promising opportunities for developing more robust early warning systems in a warming future.

Discussion

In an era of escalating weather and climate risks, early warning systems have been recognized by the World Meteorological Organization as essential tools for disaster mitigation and climate adaptation. Yet, current forecasting systems remain limited in their ability to predict extreme events at subseasonal timescale and beyond[16–20]. This study identifies three key advantages of introducing atmospheric total energy as a proxy for early warnings of extreme precipitation: (1) A substantial improvement in prediction skill at subseasonal and longer timescales. Incorporating total energy into forecast substantially enhances the accuracy of extreme precipitation prediction across regional and global scales. Compared with direct precipitation forecasts, total energy-based predictions yield up to a tenfold increase in hit rates for extreme precipitation days globally; (2) Increasing predictive value in recent years. The added skill from total energy has grown markedly since the 2010s, reflecting both a strengthened relationship between total energy and precipitation extremes and rising total energy levels under climate warming. The growing spatial coherence and intensity of large-scale extreme precipitation further amplify this signal; (3) Physical interpretability through energy budget analysis. A diagnosis of the total energy budget offers a physically grounded framework for identifying sources of predictability and model error, thus providing

https://doi.org/10.1038/s41467-026-71214-4

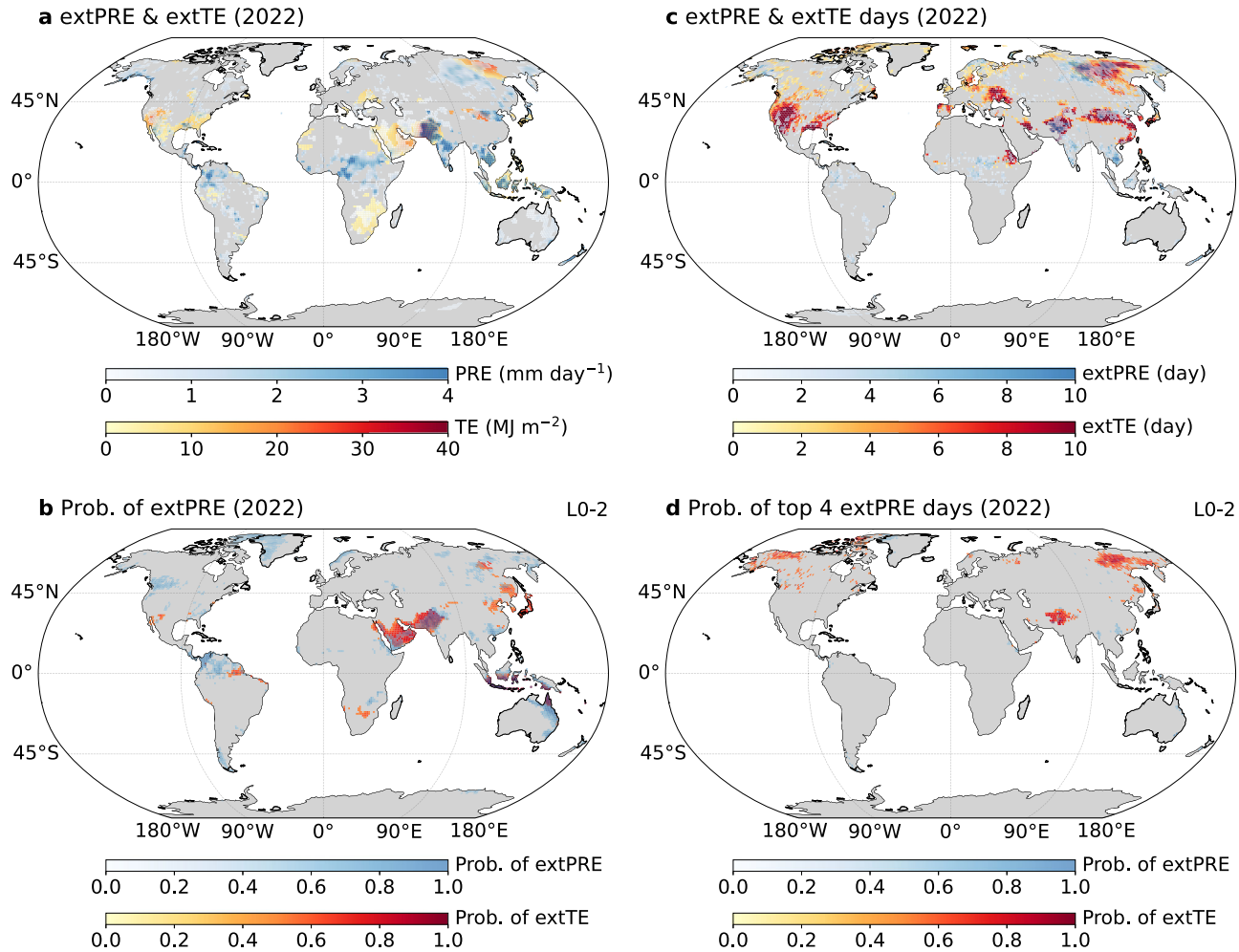


Fig. 5 | Advanced prediction of extreme precipitation via total energy-based forecasting in 2022. a Spatial distribution of observed extreme precipitation (mm day^{-1}; blue shading) and corresponding extreme total energy anomalies dominated by latent energy anomalies (MJ m^{-2}; red shading) in peak summer 2022. **b** Probabilistic prediction of extreme precipitation in 2022, from direct model output (blue shading) and total energy-based prediction (red shading). Shading is shown only where model consensus exceeds 50%. **c**, **d** Same as (**a**, **b**), but for extreme precipitation days. A year is defined as extreme when the number of extreme precipitation days ranks in the top four for the period 2005–2024. The abbreviations "PRE", "TE", "extPRE", "extTE", "Prob.", and "L0–2" denote precipitation, total energy, extreme precipitation, extreme total energy, probability, and 0–2 months leads, respectively.

guidance for detecting the forecast limit and improving forecast systems.

While existing studies have demonstrated a strong linkage between extreme precipitation and water vapor-related variables[30–34] and sought to leverage the latter's high predictability to improve regional extreme precipitation forecasts[35–38], our work suggests that total energy could serve as a more integrative proxy and offers a valuable extension to conventional moisture-based frameworks. Moreover, while winter precipitation is often considered more predictable due to its close linkage with large-scale circulation patterns[51,52], our findings highlight opportunities to improve summer extreme precipitation forecasts, where predictability has historically been lower. The applicability of total energy-based prediction, specifically whether its benefits are largely confined to summer or extend to other seasons, requires further investigation.

It should be noted that one limitation of the total energy-based prediction lies in its inability to provide accurate daily weather forecasts. This may be attributed to the fact that the release and accumulation of total energy is more directly controlled by local dynamical processes whose energy manifestations often miss detailed spatio-temporal structures. A more detailed and quantitative analysis of the relationship between extreme precipitation and total energy, and the underlying physical mechanisms, warrants further investigations. Furthermore, it is important to note that the dynamic/thermodynamic mechanisms and sources of predictability for extreme precipitation differ substantially across regions. While we have demonstrated the prediction framework's general applicability at a global scale, systematic investigations are required to quantify regional differences in the related predictive skills and to fully understand the underlying causes of these differences. Looking ahead, combining the total energy prediction with the existing numerical weather prediction models and data-driven AI weather forecasting offers a pathway toward seamless prediction across multi-scales, and the "Ready-Set-Go" early-warning concept proposed by the Red Cross Climate Centre/IRI can be finally achieved. Given that total energy integrates multiple elements representing dynamic and thermodynamic states of the atmosphere, this framework's applicability may extend beyond precipitation to other extremes such as heatwaves and severe convective storms. Exploring such applications offers a promising avenue for future research.

Methods

Observational and reanalysis datasets

Daily precipitation data is obtained from the gauge-based Climate Prediction Center (CPC) global unified precipitation dataset at

0.5° × 0.5° resolution[53]. The fifth-generation reanalysis (ERA5)[54] from the European Centre for Medium-Range Weather Forecasts (ECMWF) is adopted as a high-quality observational proxy. The ERA5 provides global data at 0.25° × 0.25° horizontal resolution and 37 vertical pressure levels from 1000 hPa to 1 hPa. The Modern-Era Retrospective Analysis for Research and Application, version 2 (MERRA-2)[55] from the National Aeronautics and Space Administration (NASA) has a 0.5° × 0.625° horizontal resolution with 42 pressure levels from 1000 hPa to 0.1 hPa. The Japanese Reanalysis for Three Quarters of a Century (JRA-3Q)[56] from the Japan Meteorological Agency (JMA) has a 0.375° × 0.375° horizontal resolution with 45 pressure levels from 1000 hPa to 0.01 hPa. The following variables are used to investigate extreme precipitation events: precipitable water, total cloud fraction, soil temperature and volumetric soil moisture (0–7 cm), surface latent and sensible heat fluxes, radiative fluxes (TOA and surface, downward and net, shortwave and longwave), temperature, specific humidity, geopotential height, and zonal, meridional, and vertical wind components. All datasets span the period 1981–2024. The coefficient of variation (Fig. 1a, b) is defined as the ratio of standard deviation to climatological mean.

The subseasonal and seasonal predictions

The ECMWF Seasonal Forecast System version 5 (SEAS5) is a fully coupled global atmosphere–land–ocean–sea ice model[57]. The SEAS5 comprises the Integrated Forecasting System (IFS, cycle 43r1) with a $T_{CO}319$ horizontal resolution (approximately 35-km) and 91 vertical levels from surface to 0.01 hPa, the Nucleus for European Modelling of the Ocean model (NEMO, v3.4) at 0.25° horizontal resolution with 75 vertical levels, the 4-level Tiled ECMWF Scheme for Surface Exchanges over Land with revised land surface hydrology (HTESSEL) shared the same horizontal resolution as the IFS, the Louvain-la-Neuve Sea Ice Model version 2 (LIM2) with a 0.5° horizontal resolution and 2 ice layers (1 snow layer), and the ECMWF wave model (ECWAN). The 7-month hindcast runs are initialized on the first day of each month from January 1981 to October 2016, with operational runs from November 2017 onward. Hindcasts and forecasts consist of 51 and 25 ensemble members, respectively. To ensure consistency, only 25 members are used for both periods in this study. Model uncertainty is captured through perturbations from both initial conditions and parameterization tendencies. Model variables used mirror those from observational datasets, including precipitation, precipitable water, cloud fraction, soil variables, heat fluxes, radiative fluxes, temperature, humidity, geopotential height, and horizontal winds. Vertical velocity is derived from the continuity equation. Lead times are defined based on the shortest and longest time intervals between initialization and target months. For example, a 0–1 month lead for peak summer (July–August) corresponds to forecasts initialized on 1 July for July targets and initialized on 1 August for August targets, and a 1–2 months lead corresponds to forecasts initialized on 1 June for July targets and initialized on 1 July for August targets. For assessing global skill in predicting peak summer (July–August) extremes, forecasts initialized on 1 May (2–4 months lead), 1 June (1–3 months lead), and 1 July (0–2 months lead) are used for targeting the entire peak summer to represent a realistic operational setting. Only the model outputs at 1° horizontal resolution are publicly available; the observational datasets are remapped to 1° when evaluating the global forecast performance.

Definition of the climatology

The number of assimilated observations in the ERA5 increased substantially after 2000 due to the launch of multiple satellites[54]. This led to marked improvements in reanalysis quality, particularly for atmospheric water vapor[58], resulting in higher accuracy of total energy, since latent energy is a key component of total energy. Consistently, a stronger correlation is observed between precipitation and total energy after 2000 (Fig. 1c), as well as between extreme precipitation days and extreme total energy days dominated by latent energy anomalies (Fig. 1d). Therefore, the most recent 20 years (2005–2024) are defined as the climatology. Seasonal anomalies (July–August) are calculated by subtracting the 2005–2024 climatological mean for each year. Daily anomalies are computed relative to the corresponding daily climatology. For the SEAS5, climatology is defined as the average of forecasts initialized on the same date from 2005 to 2024 (e.g., the average of each member of all 1 June initializations across these years). In the subseasonal predictability analysis, 3-day means are applied to variables to suppress high-frequency weather variability.

Definition of extreme precipitation events

A year is deemed extreme for precipitation or total energy during peak summer (July–August) if its seasonal mean exceeds the 2005–2024 climatological mean by more than 0.5 standard deviations. Individual days are classified as extreme when daily values surpass the 95th percentile of their climatological (2005–2024) daily values, while the daily precipitation must equal or greater than 0.1 mm. For extreme total-energy years or days, the dominant contribution—internal, latent, geopotential, or kinetic anomalies—is identified. For example, a "latent energy extreme" (inferred as extreme precipitation) denotes events where latent energy anomalies contribute most to the total energy anomalies. The thresholds to define extreme events in the SEAS5 are calculated relative to climatology, i.e., 0.5 standard deviation or 95th percentile minus daily climatology, matching the dashed lines shown in Supplementary Figs. S5–S6. The top four years during 2005–2024 with the highest counts of extreme precipitation days are classified as extreme years at each grid cell, with at least one day surpasses the climatological mean.

Direct and total energy-based predictions of extreme precipitation

An extreme precipitation year is directly predicted when the probability of precipitation anomalies exceeding the +0.5 standard deviation threshold is greater than 50% (direct precipitation prediction). For total energy-based predictions, an extreme precipitation year is predicted when the probability of total energy anomalies exceeding the +0.5 standard deviation threshold is greater than 50% (namely, introducing a total atmospheric energy proxy into forecasts), and the majority of these extreme members are dominated by latent energy anomalies. Similarly, an extreme precipitation day is directly predicted when the probability of daily precipitation anomalies exceeding the 95th percentile threshold is greater than 50%. For total energy-based predictions, a day is classified as extreme when the probability of daily total energy anomalies exceeding the 95th percentile threshold is greater than 50%, and the majority of these extreme members are dominated by latent energy anomalies. A schematic diagram of this procedure is provided in Supplementary Fig. S3.

Total energy budget diagnostics

Total energy in a specific atmospheric layer is defined as:

$$E = c_p T + L_v q + gz + \frac{1}{2}(u^2 + v^2 + w^2) \quad (1)$$

where c_p is the specific heat of dry air, T is temperature, L_v is the latent heat of vaporization, q is specific humidity, g is the gravitational constant, z is geopotential height, and u, v, and w are the three wind components. The terms from left to right on the right-hand side of Eq. (1) correspond to internal energy, latent energy, geopotential energy, and kinetic energy, respectively. To analyze the physical drivers of predictability in extreme precipitation events, the vertically integrated

total energy tendency is diagnosed as:

$$\Delta\frac{\partial\langle E\rangle}{\partial t} = -\Delta\left\langle \vec{V}_h\cdot\nabla E\right\rangle - \Delta\left\langle \omega\frac{\partial E}{\partial p}\right\rangle + \Delta\langle RAD\rangle + \Delta SH + \Delta LH - \Delta Fric \tag{2}$$

where $\vec{V}_h$ is the horizontal wind, ω is the vertical velocity, *RAD* is the net radiative flux (the sum of net shortwave and longwave radiation), *SH* is the surface upward sensible heat flux, *LH* is the surface upward latent heat flux, and *Fric* is the surface friction. Angle brackets denote mass-weighted vertical integration from the surface to the top of the atmosphere. Terms on the right-hand side of Eq. (2) represent the horizontal advection, vertical advection, net radiative heating, surface sensible heat flux, surface latent heat flux, and surface friction. Vertical integration renders vertical advection and friction negligible. The hourly ERA5 and 12-hourly SEAS5 datasets are used to calculate the total energy and solve the total energy budget equation. Because SEAS5 lacks frequent horizontal wind outputs, the horizontal advection is estimated as the residual of all other energy budget term[42]. Due to the highest output pressure level available in the SEAS5 is 10 hPa, the top of atmosphere is set to 10 hPa in both the ERA5 and the SEAS5.

Prediction skill evaluation

The hit rate (HR), Critical Success Index (CSI), and Heidke Skill Score (HSS) adopted to quantify forecast performance is expressed as:

$$HR = \frac{TP}{TP+FN} \tag{3}$$

$$CSI = \frac{TP}{TP+FN+FP} \tag{4}$$

$$HSS = \frac{2(TP\cdot TN - FP\cdot FN)}{(TP+FP)(FP+TN)+(TP+FN)(FN+TN)} \tag{5}$$

Where *TP* is the number of events where extreme precipitations are both predicted and observed, *FN* is the number of events where extreme precipitations are observed but not predicted, *FP* is the number of events where extreme precipitations are predicted but not observed, *TN* is the number of events where non-extreme precipitations are both predicted and observed. Ensemble probabilistic predictions are defined as the proportion of members forecasting an extreme event. A forecast is considered a "hit" if this probability exceeds 50%.

Data availability

The CPC global daily precipitation is publicly available at https://psl.noaa.gov/data/gridded/data.cpc.globalprecip.html. The ERA5 reanalysis dataset and the ECMWF SEAS5 seasonal prediction are publicly available at https://cds.climate.copernicus. The MERRA-2 reanalysis is publicly available at https://gmao.gsfc.nasa.gov/gmao-products/merra-2/data-access_merra-2. The JRA-3Q reanalysis is publicly available at https://gdex.ucar.edu/datasets/d640000. The data generated in this study have been deposited at https://zenodo.org/records/18925969.

Code availability

The scripts of analysis and figures are available at https://zenodo.org/records/18925969.

References

1. Allan, R. P. & Soden, B. J. Atmospheric warming and the amplification of precipitation extremes. *Science* **321**, 1481–1484 (2008).
2. Tabari, H. Climate change impact on flood and extreme precipitation increases with water availability. *Sci. Rep.* **10**, 13768 (2020).
3. Li, D., Belitz, M., Campbell, L. & Guralnick, R. Extreme weather events have strong but different impacts on plant and insect phenology. *Nat. Clim. Change* **15**, 321–328 (2025).
4. Min, S.-K., Zhang, X., Zwiers, F. W. & Hegerl, G. C. Human contribution to more-intense precipitation extremes. *Nature* **470**, 378–381 (2011).
5. Haslinger, K. et al. Increasing hourly heavy rainfall in Austria reflected in flood changes. *Nature* **639**, 667–672 (2025).
6. Donat, M. G., Lowry, A. L., Alexander, L. V., O'Gorman, P. A. & Maher, N. More extreme precipitation in the world's dry and wet regions. *Nat. Clim. Change* **6**, 508–513 (2016).
7. He, C. et al. The overlooked health impacts of extreme rainfall exposure in 30 East Asian cities. *Nat. Sustain.* **7**, 423–431 (2024).
8. Zhang, W., Zhou, T. & Wu, P. Anthropogenic amplification of precipitation variability over the past century. *Science* **385**, 427–432 (2024).
9. Hong, C.-C. et al. Causes of 2022 Pakistan flooding and its linkage with China and Europe heatwaves. *npj Clim. Atmos. Sci.* **6**, 163 (2023).
10. Nanditha, J. S. et al. The Pakistan flood of August 2022: Causes and implications. *Earth's. Future* **11**, e2022EF003230 (2023).
11. Dunstone, N. et al. Windows of opportunity for predicting seasonal climate extremes highlighted by the Pakistan floods of 2022. *Nat. Commun.* **14**, 6544 (2023).
12. Zhang, W. et al. A year marked by extreme precipitation and floods: weather and climate extremes in 2024. *Adv. Atmos. Sci.* **42**, 1045–1063 (2025).
13. Green, A. C., Fowler, H. J., Blenkinsop, S. & Davies, P. A. Precipitation extremes in 2024. *Nat. Rev. Earth Environ.* **6**, 243–245 (2025).
14. Li, C., Liu, J., Du, F., Zwiers, F. W. & Feng, G. Increasing certainty in projected local extreme precipitation change. *Nat. Commun.* **16**, 850 (2025).
15. Bao, J., Sherwood, S. C., Alexander, L. V. & Evans, J. P. Future increases in extreme precipitation exceed observed scaling rates. *Nat. Clim. Change* **7**, 128–132 (2017).
16. Vitart, F. et al. The subseasonal to seasonal (S2S) prediction project database. *Bull. Am. Meteorol. Soc.* **98**, 163–173 (2017).
17. Vitart, F. & Robertson, A. W. The sub-seasonal to seasonal prediction project (S2S) and the prediction of extreme events. *npj Clim. Atmos. Sci.* **1**, 3 (2018).
18. Borodina, A., Fischer, E. M. & Knutti, R. Models are likely to underestimate increase in heavy rainfall in the extratropical regions with high rainfall intensity. *Geophys. Res. Lett.* **44**, 7401–7409 (2017).
19. Sillmann, J. et al. Understanding, modeling and predicting weather and climate extremes: challenges and opportunities. *Weather Clim. Extrem.* **18**, 65–74 (2017).
20. Malik, I., Chuphal, D. S., Vegad, U. & Mishra, V. Was the extreme rainfall that caused the August 2022 flood in Pakistan predictable? *Environ. Res. Clim.* **2**, 4 (2023).
21. Chen, L. et al. A machine learning model that outperforms conventional global subseasonal forecast models. *Nat. Commun.* **15**, 6425 (2024).
22. Lyu, Y. et al. Improving subseasonal-to-seasonal prediction of summer extreme precipitation over southern China based on a deep learning method. *Geophys. Res. Lett.* **50**, e2023GL106245 (2023).
23. Das, P. et al. Hybrid physics-AI outperforms numerical weather prediction for extreme precipitation nowcasting. *npj Clim. Atmos. Sci.* **7**, 282 (2024).

24. Herman, G. R. & Schumacher, R. S. Money doesn't grow on trees, but forecasts do: Forecasting extreme precipitation with random forests. *Mon. Weather Rev.* **146**, 1571–1600 (2018).
25. Price, I. et al. Probabilistic weather forecasting with machine learning. *Nature* **637**, 84–90 (2025).
26. Zhang, Y. et al. Skillful nowcasting of extreme precipitation with NowcastNet. *Nature* **619**, 526–532 (2023).
27. De Vries, A. J. et al. Breaking Rossby waves drive extreme precipitation in the world's arid regions. *Commun. Earth Environ.* **5**, 493 (2024).
28. Cheng, T. F., Wang, B., Liu, F., Chen, G. & Lu, M. Shifts in MJO behavior enhance predictability of subseasonal precipitation whiplashes. *Nat. Commun.* **16**, 3978 (2025).
29. Richter, J. H. et al. Quantifying sources of subseasonal prediction skill in CESM2. *npj. Clim. Atmos. Sci.* **7**, 59 (2024).
30. Held, I. M. & Soden, B. J. Robust responses of the hydrological cycle to global warming. *J. Clim.* **19**, 5686–5699 (2006).
31. Trenberth, K. E., Dai, A., Rasmussen, R. M. & Parsons, D. B. The changing character of precipitation. *Bull. Am. Meteorol. Soc.* **84**, 1205–1218 (2003).
32. O'Gorman, P. A. & Schneider, T. The physical basis for increases in precipitation extremes in simulations of 21st-century climate change. *Proc. Natl. Acad. Sci. USA* **106**, 14773–14777 (2009).
33. Kim, S., Sharma, A., Wasko, C. & Nathan, R. Linking total precipitable water to precipitation extremes globally. *Earth's. Future* **10**, e2021EF002473 (2022).
34. Kim, S., Wasko, C., Sharma, A. & Nathan, R. The role of regional water vapor dynamics in creating precipitation extremes. *J. Hydrol. X* **24**, 100181 (2024).
35. Kingston, D. G., Cooper, L., Lavers, D. A. & Hannah, D. M. Brief communication: forecasting extreme precipitation from atmospheric rivers in New Zealand. *Nat. Hazards Earth Syst. Sci.* **25**, 675–682 (2025).
36. Lavers, D. A., Pappenberger, F. & Zsoter, E. Extending medium-range predictability of extreme hydrological events in Europe. *Nat. Commun.* **5**, 5382 (2014).
37. Reid, K. J., Hudson, D., King, A. D., Lane, T. P. & Marshall, A. G. Atmospheric water vapour transport in ACCESS-S2 and the potential for enhancing skill of subseasonal forecasts of precipitation. *Q. J. R. Meteorol. Soc.* **150**, 68–80 (2023).
38. Wang, S. & Yuan, X. Extending seasonal predictability of Yangtze River summer floods. *Hydrol. Earth Syst. Sci.* **22**, 4201–4211 (2018).
39. Gu, L. et al. Large anomalies in future extreme precipitation sensitivity driven by atmospheric dynamics. *Nat. Commun.* **14**, 3197 (2023).
40. Ou, Q. et al. Relating extreme precipitation events to atmospheric conditions and driving variables in China. *Clim. Dyn.* **62**, 4925–4942 (2024).
41. Ghausi, S. A., Zehe, E., Ghosh, S., Tian, Y. & Kleidon, A. Thermodynamically inconsistent extreme precipitation sensitivities across continents driven by cloud-radiative effects. *Nat. Commun.* **15**, 10669 (2024).
42. Zhang, T., Deng, Y., Chen, J., Yang, S. & Dai, Y. An energetics tale of the 2022 mega-heatwave over central-eastern China. *npj Clim. Atmos. Sci.* **6**, 162 (2023).
43. Trenberth, K. E. & Fasullo, J. T. Regional energy and water cycles: Transports from ocean to land. *J. Clim.* **26**, 7837–7851 (2013).
44. Wang, R. & Chen, G. A conceptual model of diurnal recharge–discharge of energy for the record-breaking heavy rains over East Asia in summer 2020. *Mon. Weather Rev.* **153**, 1195–1217 (2025).
45. Yang, M., Shi, X., Yuan, C., Lu, X. & Liu, J. Summer extreme precipitation in southern China from the perspective of moisture static energy. *J. Clim.* **36**, 4967–4986 (2023).
46. Wang, Z., Luo, H. & Yang, S. Different mechanisms for the extremely hot central-eastern China in July–August 2022 from a Eurasian large-scale circulation perspective. *Environ. Res. Lett.* **18**, 024023 (2023).
47. He, C., Zhou, T., Zhang, L., Chen, X. & Zhang, W. Extremely hot East Asia and flooding western South Asia in the summer of 2022 tied to reversed flow over Tibetan Plateau. *Clim. Dyn.* **61**, 2103–2119 (2023).
48. Ma, Q. et al. Multiscale interaction underlying 2022 concurrent extreme precipitation in Pakistan and heatwave in Yangtze River Valley. *npj Clim. Atmos. Sci.* **7**, 177 (2024).
49. Doi, T., Behera, S. K. & Yamagata, T. Seasonal predictability of the extreme Pakistani rainfall of 2022 possible contributions from the northern coastal Arabian Sea temperature. *npj Clim. Atmos. Sci.* **7**, 13 (2024).
50. Takahashi, H. G. Role of tropical disturbances along the South Asian monsoon trough in the 2022 Pakistan floods and the implications for interannual variability. *J. Clim.* **37**, 5609–5627 (2024).
51. Liu, Y., Hu, Z.-Z. & Wu, R. Cooperative effects of tropical Pacific and Atlantic SST forcing in southern China winter precipitation variability. *Clim. Dyn.* **55**, 2903–2919 (2020).
52. Horan, M. F., Kucharski, F., Johnson, N. & Ashfaq, M. Winter precipitation predictability in Central Southwest Asia and its representation in seasonal forecast systems. *npj Clim. Atmos. Sci.* **7**, 80 (2024).
53. Chen, M. et al. Assessing objective techniques for gauge-based analyses of global daily precipitation. *J. Geophys. Res. Atmos.* **113**, D04110 (2008).
54. Hersbach, H. et al. The ERA5 global reanalysis. *Q. J. R. Meteorol. Soc.* **146**, 1999–2049 (2020).
55. Gelaro, R. et al. The modern-era retrospective analysis for research and applications, version 2 (MERRA-2). *J. Clim.* **30**, 5419–5454 (2017).
56. Kosaka, Y. et al. The JRA-3Q reanalysis. *J. Meteor. Soc. Jpn.* **102**, 49–109 (2024).
57. Johnson, S. J. et al. SEAS5: The new ECMWF seasonal forecast system. *Geosci. Model Dev.* **12**, 1087–1117 (2019).
58. Mayer, J., Mayer, M. & Haimberger, L. Consistency and homogeneity of atmospheric energy, moisture, and mass budgets in ERA5. *J. Clim.* **34**, 3955–3974 (2021).

Acknowledgements

T.Z. and S.Y. are supported by the Guangdong Major Project of Basic and Applied Basic Research (2020B0301030004), the Southern Marine Science and Engineering Guangdong Laboratory (Zhuhai) (SML2024SP012), and the Guangdong Province Key Laboratory for Climate Change and Natural Disaster Studies (2023B1212060019). Y.D. is supported by the U.S. National Science Foundation (NSF) through Grant AGS-2032532 and by the U.S. National Oceanic and Atmospheric Administration (NOAA) through Grant NA22OAR4310606. D.C. is supported by Carbon Neutrality and Energy System Transformation (CNEST) Program and Tsinghua University (100008001).

Author contributions

T.Z. and Y.D. conceived and designed the study. T.Z. conducted the data analysis and drafted the first manuscript. J.C. conducted the data analysis, provided comments, and revised the manuscript. Y.D., S.Y., D.C., and F.C. provided comments and revised the manuscript. J.Z. conducted the data analysis. All authors discussed the scientific interpretation of the results.

Competing interests

The authors declare no competing interests.

Additional information

Supplementary information The online version contains supplementary material available at https://doi.org/10.1038/s41467-026-71214-4.

Correspondence and requests for materials should be addressed to Tuantuan Zhang or Yi Deng.

Peer review information *Nature Communications* thanks the anonymous reviewers for their contribution to the peer review of this work. A peer review file is available.

Reprints and permissions information is available at http://www.nature.com/reprints

Publisher's note Springer Nature remains neutral with regard to jurisdictional claims in published maps and institutional affiliations.

Open Access This article is licensed under a Creative Commons Attribution-NonCommercial-NoDerivatives 4.0 International License, which permits any non-commercial use, sharing, distribution and reproduction in any medium or format, as long as you give appropriate credit to the original author(s) and the source, provide a link to the Creative Commons licence, and indicate if you modified the licensed material. You do not have permission under this licence to share adapted material derived from this article or parts of it. The images or other third party material in this article are included in the article's Creative Commons licence, unless indicated otherwise in a credit line to the material. If material is not included in the article's Creative Commons licence and your intended use is not permitted by statutory regulation or exceeds the permitted use, you will need to obtain permission directly from the copyright holder. To view a copy of this licence, visit http://creativecommons.org/licenses/by-nc-nd/4.0/.

© The Author(s) 2026